

Transition Induced by a Streamwise Array of Roughness Elements on a Supersonic Flat Plate

Amanda Chou* and Michael A. Kegerise†

NASA Langley Research Center, Hampton, VA, 23681, USA

Roughness is unavoidable on practical high-speed vehicles, so it is critical to determine its impact on boundary layer transition. The flow field downstream of a streamwise array of cylindrical roughness elements is probed with hot-wire anemometry in this experiment. Mean flow distortion is examined in several measurement planes in the wake of the cylindrical roughness using the streak strength profiles and contour plots of the mass flux and total temperature. The roughness element heights and spacings were varied and their instability modes were examined. Cylindrical roughness elements approximately $140\text{ }\mu\text{m}$ tall produce an odd instability mode that grows weakly with downstream distance in the measurement range of this experiment. Cylindrical roughness elements approximately $280\text{ }\mu\text{m}$ tall produce an even instability mode that grows, becomes nonlinear, and then breaks down. Transition onset remains constant relative to the most downstream roughness in the streamwise array when the $280\text{ }\mu\text{m}$ roughness elements are spaced 2 diameters apart. Transition onset occurs at an earlier upstream location relative to the most downstream roughness in the streamwise array when the roughness elements are spaced 4 diameters apart. The wake behind roughness elements spaced 2 diameters apart do not appear to recover before the next downstream roughness element, so the location of transition shifts with the location of the most downstream roughness element in the array. When the roughness elements are spaced 4 diameters apart, the flow behind the first roughness element has enough space to recover before feeding into the second roughness element, and thus, moves transition forward.

I. Introduction

The subject of roughness-induced transition in high-speed flows is of concern for practical geometries and vehicles. Manufactured surfaces have an inherent distributed roughness and fasteners or sensors can become a pattern of isolated roughness elements. These real-life features can make an otherwise smooth surface rough. Given that roughness is an unavoidable circumstance on practical vehicles, it is critical to determine its impact on boundary-layer transition. To that end, the physical mechanisms by which roughness causes transition must be better understood and incorporated into transition models. The onset of transition may be caused by a variety of factors including the enhancement of receptivity to the external disturbances,¹ the transient growth of boundary-layer perturbations, the acceleration of the growth of existing instability modes in the boundary layer,² and the wake instabilities induced by the roughness itself.³⁻⁶

Much of the high-speed literature concerns the sizing of roughness trips to induce transition. The knowledge of the sizing of an effective trip can help designers determine an acceptable limit for manufacturing tolerances. Large isolated roughness elements can cause transition through the production of a wake instability driven by an absolute instability upstream. Smaller isolated roughness elements can cause transition by amplifying a boundary layer instability present upstream even when the integrated growth potential of the wake instability is not enough to incite transition.² Work has also been done on the use of discrete roughness elements to modulate the boundary layer in order to delay transition. Spanwise arrays of discrete roughness elements have been used on swept wings to excite a stable wavelength of crossflow vortices on swept wings⁷⁻¹⁰ and on cones.¹¹⁻¹⁴ These passive methods of control can be effective, but the design of these

*Research Aerospace Engineer, Flow Physics & Control Branch, M/S 170, AIAA Senior Member.

†Research Scientist, Flow Physics & Control Branch, M/S 170, AIAA Senior Member.

patterns of arrays could benefit from a deeper understanding of the underlying physics that make them effective.

The study of the physics of pseudo-random distributed roughness has been extensively carried out in subsonic flow by an experimental group at Texas A&M University^{15–17} and a computational group at University of Texas.^{18–20} Much of this work has shown that a distributed roughness pattern seems to be defined primarily by its most prominent features^{15,18} and that the presence of a distributed roughness can shield an isolated roughness.¹⁷ Careful design of the surface roughness and careful probing of the flow field behind the roughness patterns in the Klebanoff-Saric Wind Tunnel at Texas A&M University have produced measurements that can be compared to matching computations.^{15,17,18}

Studies of arrays of isolated roughness elements can provide insight into the interaction of features in a distributed roughness pattern. By roughly approximating a distributed roughness pattern as a grid or array of isolated roughness elements, information may be gleaned about the underlying interaction between these most prominent features. Historic work by Carmichael measured the transition Reynolds number on a flat plate due to the presence of arrays of roughness elements in a subsonic facility.²¹ Noting that the parametric space to study was large, Carmichael investigated the effect of grids of cylindrical roughness elements, streamwise rows of roughness, and spanwise rows of roughness. Carmichael also varied the heights and diameters of the roughness elements in the different configurations. Carmichael found that there was less of an effect, and likely, less interaction between roughness elements spaced more than 4 diameters apart in the streamwise direction. However, the interaction between cylindrical roughness elements with the same height seemed to be at a maximum when they were spaced 2 diameters apart from center to center in the streamwise direction.

Choudhari et al. looked at the effect of two tandem roughness trips with diamond-shaped planforms in a Mach 3.5 flow configuration similar to the Supersonic Low Disturbance Tunnel at NASA Langley Research Center.²² These roughness trips were diamond shaped, with heights of 0.004 inches and 0.010 inches, a width of 0.05 inches, and spaced 0.1575 inches apart from center to center in the streamwise direction. The computations examined the effect of height on the amplitude of the streaks downstream of the roughness trips induced by the wake instability. The addition of a downstream isolated roughness had an effect on the streak amplitude when the roughness was short ($k/\delta_{0.995} = 0.15$) and less of an effect on the streak amplitude when the roughness was taller ($k/\delta_{0.995} = 0.37$). Choudhari et al. propose that this is due to the ability of the flow field to recover after the first roughness trip and the receptivity of the second roughness trip to the wake behind the first roughness trip.

The wakes of several different roughness planforms were carefully probed with a hot wire in Ref. 6 to determine mode shapes present behind these different roughness elements. These mode shapes were similar to those that were previously computed by Choudhari et al.² The comparison of these two studies shows that the capturing of a complex instability field can help to validate the computational tools being developed to predict transition. The following experiment continues the study of this complex flow field behind the roughness, by studying the effect of streamwise arrays of cylindrical roughness.

II. Facility and Equipment

A highly-polished flat plate with a nominally sharp leading edge was tested in the NASA Langley Research Center (LaRC) Supersonic Low Disturbance Tunnel (SLDT), a Mach-3.5 quiet facility. A two-dimensional nozzle with exit dimensions of 15.24 cm by 25.40 cm (6 in. by 10 in.) was used in the SLDT for these experiments. As a quiet tunnel, greater control over the freestream disturbance level is possible in this facility, ensuring that measurements are not influenced by these outside parameters. Existing infrastructure (compressors, vacuum pumps, vacuum spheres, etc.) enables the facility to be run for extended periods of time. At sufficiently low freestream conditions, this run time can be on the order of hours. The extended run time and disturbance level of the facility enables extensive probing of the flow field of the models used and allows for the model to reach an equilibrium temperature before the flow field is examined.

Measurements of the freestream mass-flux fluctuations in the SLDT were made with two normal hot wires spaced 0.4 mm apart. These wires were oriented so that each sensing element was approximately perpendicular to the flat sidewalls of the nozzle. These hot wires were platinum-plated tungsten wires that are 5 μm in diameter and approximately 1 mm long. These measurements were made with a constant temperature anemometer with a symmetric bridge and an overheat ratio of 0.75. The signals were sampled at 500 kHz for two seconds after passing through a signal conditioner with a low-pass filter cutoff at 200 kHz

and a high-pass filter cutoff at 100 Hz. Mean measurements of the hot-wire voltage were recorded with a digital voltmeter.

The data shown in Fig. 1 correspond to the hot-wire measurements that were made along the centerline of the SLDT. These data are plotted against x , which is the distance from the nozzle throat in this case. The RMS mass-flux fluctuations are plotted in the top figure and a dashed line at 0.1% indicates the threshold above which the flow is no longer considered to be “quiet.” The uncorrelated noise between the two sensors is removed through a cross-spectral analysis and the resulting RMS fluctuations in the freestream mass flux are plotted for four different stagnation pressures. As the stagnation pressure increases, the location where increased freestream fluctuations are greater than 0.1% of the mean moves upstream. The mean mass flux is plotted on the bottom figure in Fig. 1 and shows that the flow becomes uniform at a location approximately 12.5 cm from the throat. The performance of the nozzle is similar to the performance measured in 2013.⁶

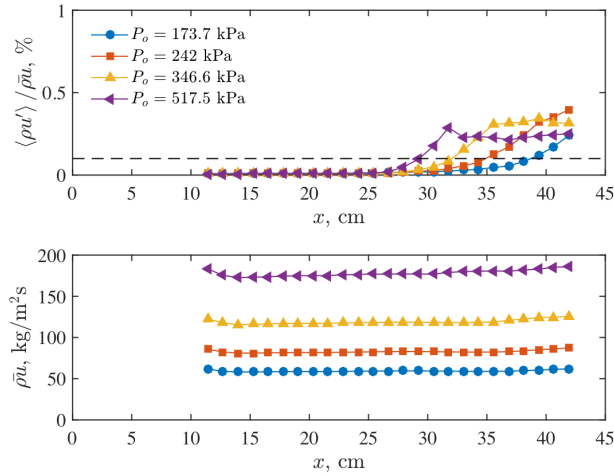


Figure 1. Measurements with dual normal hot wires of the RMS mass-flux fluctuations and mean mass-flux fluctuations along the centerline of the SLDT: $M = 3.5$, $T_0 = 319.3$ K.

A. Flat Plate Model

The flat plate model was positioned so that the leading edge of the plate is 14 cm from the nozzle throat, well in the region where uniform flow is expected. The flat plate is 228.6 mm wide at the leading edge, 76.2 mm at the trailing edge, and 406.4 mm long. The upper surface of the plate, where measurements are made, is polished to a mirror finish ($0.025 \mu\text{m}$ RMS roughness). A picture of the flat plate model is provided in Fig. 2.



Figure 2. A side view of the polished flat plate. Measurement surface is toward the top of the picture.

B. Roughness Elements

Circular cylindrical roughness elements (CREs) were used in the experiments presented in this paper (Fig. 3). The cylindrical roughness elements tested were nominally 3.58 mm in diameter. Two nominal heights of the CREs were tested: 140- μm and 280- μm . The height of each of the roughness elements was measured with

a stylus-based surface profilometer. An example of the measurement of the height of one of the roughness elements is provided in Fig. 4. Actual heights of the roughness elements ranged from $137\text{ }\mu\text{m}$ to $143.5\text{ }\mu\text{m}$ for the shorter of the roughness elements and from $270\text{ }\mu\text{m}$ to $287\text{ }\mu\text{m}$ for the taller of the roughness elements.

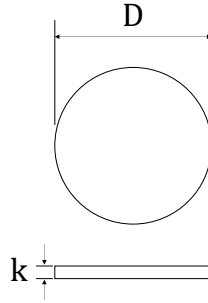


Figure 3. A schematic of the circular CREs used and relevant dimensions (not to scale).

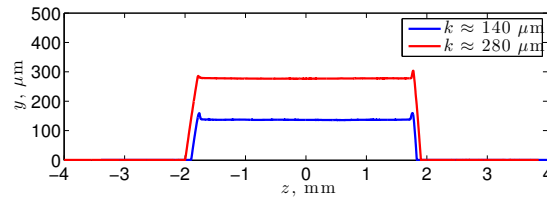


Figure 4. An example of the measured height of a roughness element applied to the surface of the flat plate.

A schematic of the positioning of the roughness elements on the flat plate is given in Fig. 5. Measurements downstream of the roughness element may be referenced to the most downstream element, which is centered at a position of x_0 from the leading edge of the flat plate. Measurements relative to the leading edge are given by their x -coordinate.

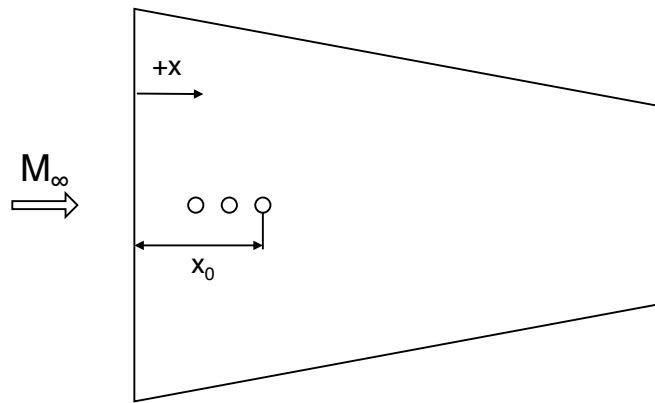


Figure 5. A schematic of the relative positioning of the roughness elements on the flat plate (not to scale).

These roughness elements were positioned so that the farthest upstream roughness element was centered at a location of 41.5 mm from the leading edge of the flat plate. A template was used to align the roughness elements on the flat plate and each roughness element was affixed with a cyanoacrylate glue. The distances between each roughness element were fixed by the template at a center-to-center spacing of two diameters ($2D$) apart or four diameters ($4D$) apart for the CREs. Additional roughness elements were mounted downstream of the first element, spacing them $2D$ apart until a total of three elements were in line, and then

removing the center element to test a spacing of $4D$ apart. This ensured that the element at the upstream position was constant throughout the experiment. Larger spacings between the roughness elements were not attempted due to the limited measurement region where the flow on the flat plate was not disturbed by increased freestream noise or effects of the edges of the flat plate.

Hot-wire anemometry was also used to probe the boundary layer. A symmetric bridge was used in the same anemometer used to make freestream measurements. The sensing element used in the boundary layer probes was a $3.8\text{-}\mu\text{m}$ platinum-plated tungsten wire with a nominal length of 0.5 mm . The wire was tuned such that the square wave response provides a frequency bandwidth of approximately 370 kHz . The hot wire was set to a high overheat ratio of 0.75 in order to be primarily sensitive to mass flux. The cold-wire resistance was also measured at each measurement station in order to correct for the total-temperature change in the boundary layer. The measurements were passed through a signal conditioner that had a low-pass filter cutoff at 400 kHz and a high-pass filter cutoff at 100 Hz . The signal was sampled at 1 MHz for one second at each measurement location.

III. Analysis

The effect of the different roughness configurations was analyzed by using both static (mean) and dynamic data. Profiles of the mass flux and total temperature across the boundary layer yielded insight into the mean flow distortion in the wake. The mean data are presented in the paper as contour plots of mass flux and total temperature as well as profiles of the streak strength downstream of the roughness. The dynamic data are analyzed as estimates of the power spectral density and the RMS fluctuations behind the roughness. The power spectra can show the particular frequency of interest in the wake of the roughness. The RMS fluctuations yield a clearer picture of the instability modes associated with the frequencies of interest.

The freestream total pressure and total temperature were held at $207.4 \pm 0.38\text{ kPa}$ and $319.3 \pm 0.16\text{ K}$, respectively, for all of the data points collected. The distances in the streamwise direction are normalized by the location of the most downstream roughness element, x_0 , and again by the number of diameters D that correspond with this distance. The full planar surveys at each x location contained up to 777 points. The collection of these full planar surveys was time consuming, so some of the measurement stations only include partial planes.

A. Measurements of Mass Flux and Total Temperature in the Boundary Layer

Profiles of the mass flux and total temperature were taken downstream of the roughness element. The mass flux was computed from the measured voltage using a calibration of the hot wire at multiple Reynolds numbers, as given in Fig. 6(a). In Fig. 6(a), T_0 is the mean total temperature at which the hot-wire measurement was made. The total temperature was determined using an iterative method. First, a recovery factor (η) for the wire was estimated using the assumed freestream or edge value. Next, the recovery temperature was calculated using the measured cold-wire resistance (R_r) using

$$T_r = T_{ref} + \frac{1}{\alpha} \left(\frac{R_r}{R_{ref}} - 1 \right) \quad (1)$$

where R_{ref} is the wire resistance at the reference temperature T_{ref} and α is the temperature coefficient of resistance for platinum-plated tungsten. The initial estimate for the total temperature in the boundary layer was taken to be the value corresponding with the estimated recovery factor: $T_0 = T_r/\eta$. Using the measured voltage (E_0) and the estimated total temperature, the mass flux (ρu) can be computed using the calibration given in Fig. 6(a) and the wire Reynolds number can be computed using

$$Re_d = \frac{\rho u d}{\mu_0} \quad (2)$$

where d is the diameter of the hot wire and μ_0 is the viscosity based on the total temperature, using a Sutherland law. Then, using the cold-wire calibration given in Fig. 6(b), a new wire recovery factor is estimated and the process is repeated until the mass flux and total temperature converge to a constant value. Further details on the method of calibration used can be found in Ref. 23.

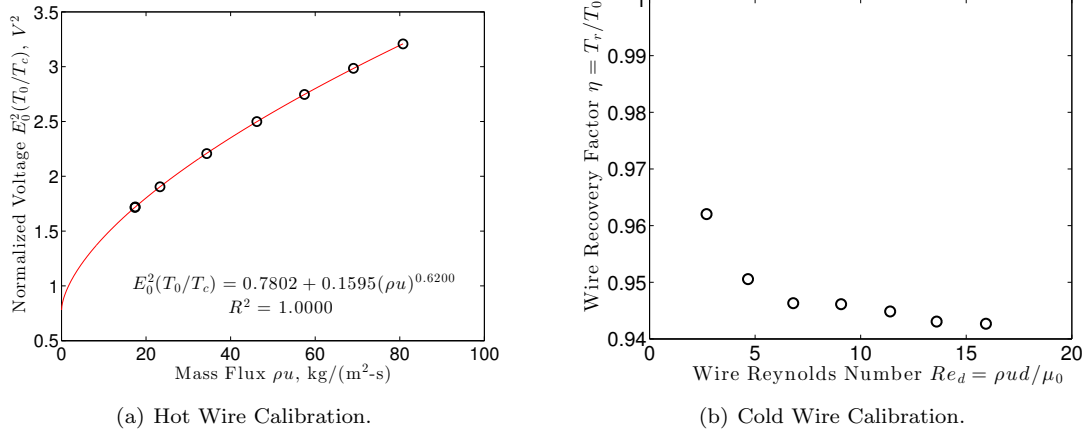


Figure 6. Example hot wire calibration for boundary layer probes.

B. Streak Amplitudes

The mean flow distortion in the wake of roughness elements can be given by the relative amplitude of the high-speed and low-speed regions behind the roughness. The streak amplitude is defined by Fransson et al. as the wall-normal maximum of the peak-to-peak difference between the streamwise velocities:

$$A_{ST} = \frac{1}{2} \max_y \left\{ U(y)_{high} - U(y)_{low} \right\} \quad (3)$$

where $U(y)_{high}$ and $U(y)_{low}$ are the velocity profiles in a high-speed and low-speed streak region, respectively.²⁴ Unlike Fransson's case, the streak strength in this paper is based on ρu because the hot-wire measurements are sensitive to mass flux in compressible flow. For these data, a streak strength is defined as

$$A_{\rho u} = \frac{1}{2} \left(\rho u(y)_{high} - \rho u(y)_{low} \right) \quad (4)$$

and the streak amplitude is defined as the wall-normal maximum of the streak strength profile. These streak strength profiles are nondimensionalized by the edge mass flux of the profiles and the height in the boundary layer is nondimensionalized by the boundary layer parameter

$$\eta = y \sqrt{\frac{Re}{x}} \quad (5)$$

where y is the height above the surface of the flat plate and Re is the freestream unit Reynolds number.

C. Power Spectra and RMS Mass Flux

The power spectra were determined using the Welch spectrum estimation method, applying Blackman windows to 1024-point windows, allowing up to 50% overlap in the windows, and then averaging the samples over the one-second period. These parameters yielded a frequency spacing of 976.6 Hz. The RMS mass-flux fluctuations were determined by taking the power spectra of the mass-flux fluctuations, integrating along a 5 kHz bandwidth around the frequency of interest, and then taking the square root of the integrated value. For each planar survey behind the roughness element, a 5-kHz bandwidth was investigated for several frequencies between 20 kHz and 95 kHz for each measurement location. The maximum RMS amplitude of mass flux in this band was used to determine the frequency of wake instabilities of interest. Contour plots of these particular frequencies were then made to determine the shape of the instability modes and the location at which these modes were concentrated. The peak RMS amplitude was then computed for each planar survey in the region where the instability modes were concentrated and plotted to show the growth of the instability downstream.

IV. Results

The boundary layer and streak strength profiles show the amount of mean-flow distortion caused by the presence of roughness elements. The streak amplitude offers less information about the actual growth of instabilities. Power spectra are used to identify the instabilities present in the boundary layer behind the roughness elements and contour maps of planes behind the roughness elements are used to map the mode shapes of the instabilities. The spectra and contour maps provide more details on the underlying physics of the transition process.

A. Mean Profiles of Mass Flux and Temperature Downstream of Roughness

The profiles of mean mass flux for roughness elements with $k \approx 140 \mu\text{m}$ are given in Figs. 7, 9, 11, and 13. The configurations corresponding with these profiles are a single roughness element at $x_0 = 41.5 \text{ mm}$, two roughness elements spaced $2D$ apart, three roughness elements spaced $2D$ apart, and two roughness elements spaced $4D$ apart, respectively. The profiles of mean total temperature for the same height of CRE and same configurations are given in Figs. 8, 10, 12, and 14. Only two streamwise stations are shown here due to the similarity in measurements at each downstream station. In general, these show weak flow distortion in the mass flux behind the CREs, regardless of the number of elements and the spacing between the elements. The presence of two hot streaks in the total temperature profiles is slightly visible in the most downstream contour map (Figs. 8(b), 10(b), 12(b), and 14(b)).

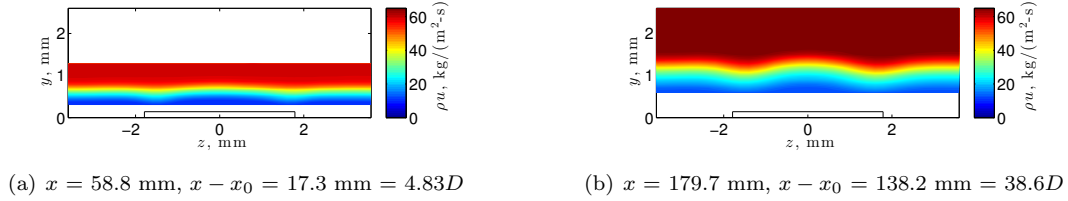


Figure 7. Mean mass flux behind one CRE located at $x_0 = 41.5 \text{ mm}$ ($k \approx 140 \mu\text{m}$).

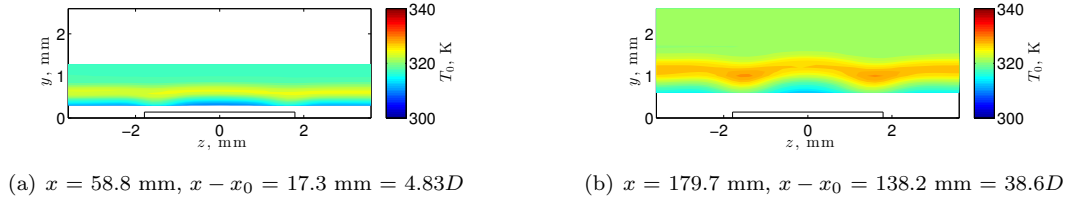


Figure 8. Mean total temperature behind one CRE located at $x_0 = 41.5 \text{ mm}$ ($k \approx 140 \mu\text{m}$).

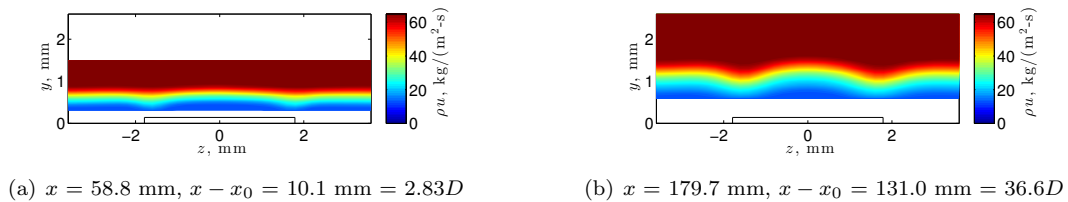


Figure 9. Mean mass flux behind two CREs, spaced $2D$ apart, with the last element centered at $x_0 = 48.7 \text{ mm}$ ($k \approx 140 \mu\text{m}$).

Spanwise planar profiles of the flow field downstream of taller CREs with heights of approximately $280 \mu\text{m}$ are given in Figs. 15–22. These are presented as a mass flux profile and then a total temperature profile for the following configurations, respectively: one roughness element at $x_0 = 41.5 \text{ mm}$, two roughness elements spaced $2D$ apart, three roughness elements spaced $2D$ apart, and two roughness elements spaced $4D$ apart.

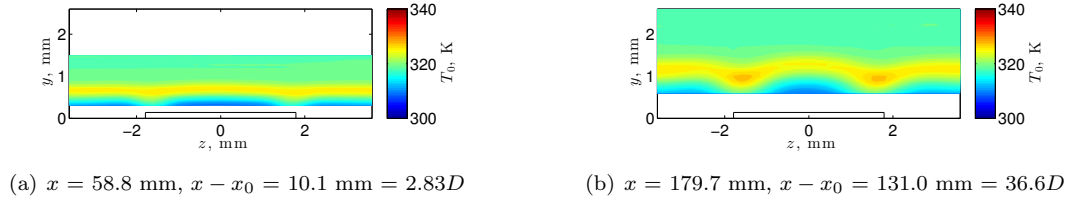


Figure 10. Mean total temperature behind two CREs, spaced $2D$ apart, with the last element centered at $x_0 = 48.7 \text{ mm}$ ($k \approx 140 \mu\text{m}$).

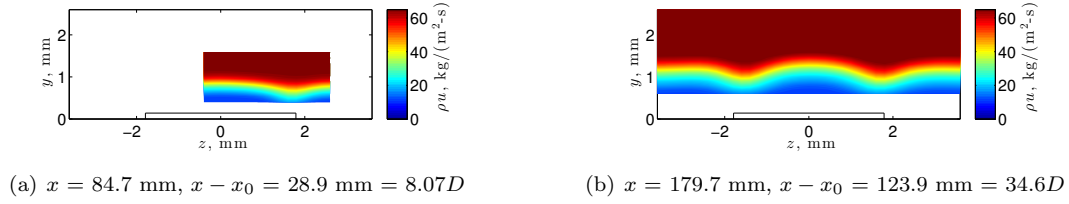


Figure 11. Mean mass flux behind three CREs, each spaced $2D$ apart, with the last element centered at $x_0 = 55.8 \text{ mm}$ ($k \approx 140 \mu\text{m}$).

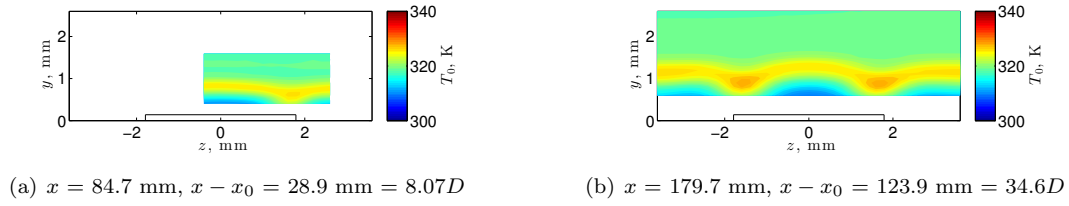


Figure 12. Mean total temperature behind three CREs, each spaced $2D$ apart, with the last element centered at $x_0 = 55.8 \text{ mm}$ ($k \approx 140 \mu\text{m}$).

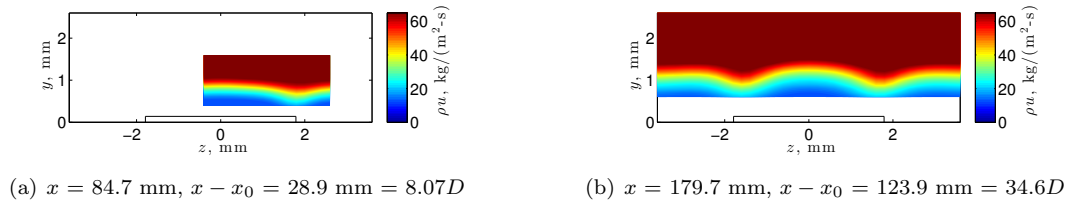


Figure 13. Mean mass flux behind two CREs, spaced $4D$ apart, with the last element centered at $x_0 = 55.8 \text{ mm}$ ($k \approx 140 \mu\text{m}$).

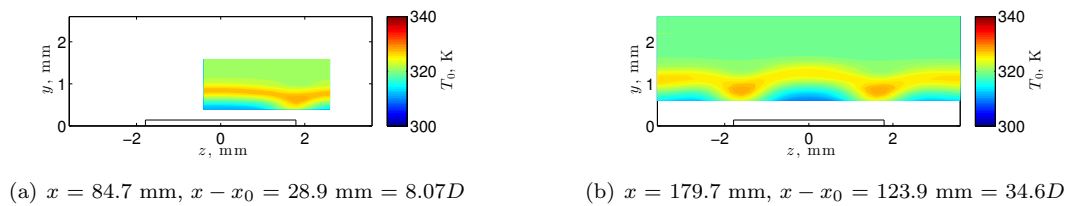


Figure 14. Mean total temperature behind two CREs, spaced $4D$ apart, with the last element centered at $x_0 = 55.8 \text{ mm}$ ($k \approx 140 \mu\text{m}$).

The mean mass flux profiles in Figs. 15, 17, 19, and 21 show much more distortion in the wake of the taller roughness elements than in the wake of the 140- μm -tall roughness elements. There is a greater difference in amplitude in the regions where mass flux is at a maximum compared to the regions where mass flux is at a minimum. For each of the arrays where the roughness elements are only spaced $2D$ apart, the mean mass flux and the mean total temperature start to show less distortion at $x = 218.4$ mm (Figs. 15(d) and 16(d), 17(d) and 18(d), and 19(d) and 20(d)). This could indicate that transition is occurring on the flat plate and will be shown in Section C. The configuration with two taller roughness elements spaced $4D$ apart (Figs. 21(c) and 22(c)) shows that the mean flow in the wake of the roughness elements begin to lose distortion and become more uniform at a measurement station upstream of $x = 179.7$ mm. Inspection of the RMS fluctuations of the mass flux will show that the flow is starting to transition at this station.

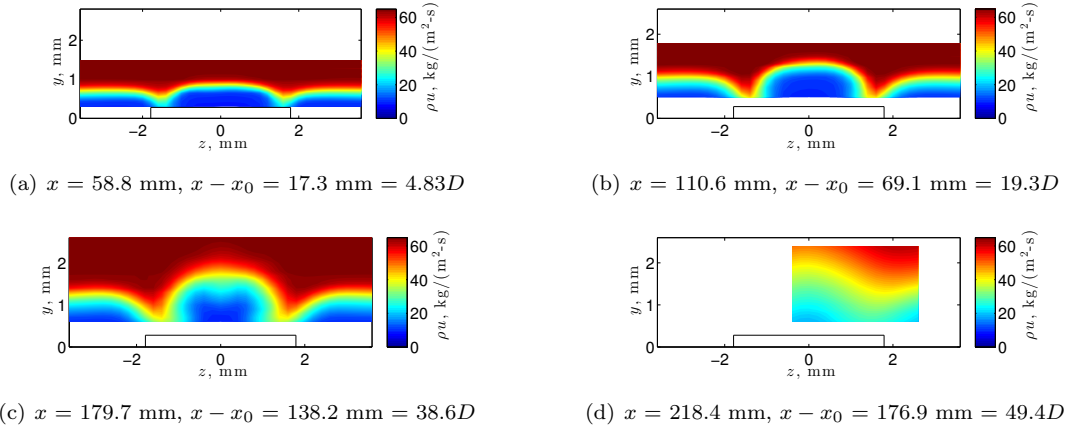


Figure 15. Mean mass flux behind one CRE located at $x_0 = 41.5$ mm ($k \approx 280$ μm).

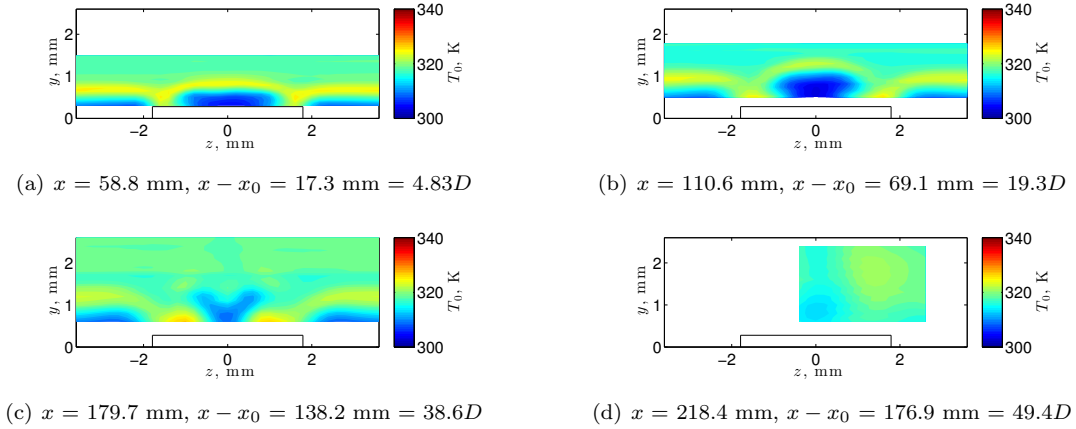


Figure 16. Mean total temperature behind one CRE located at $x_0 = 41.5$ mm ($k \approx 280$ μm).

B. Streak Amplitudes

The streak strengths of the different roughness configurations were analyzed at varying distances downstream of the roughness elements using Equation 4. Fig. 23 shows the streak strength profiles behind streamwise arrays of CREs that are approximately 140 μm tall. The farthest upstream station at which measurements could be made show a maximum in the streak strength at a location in the middle of the boundary layer. This peak grows in amplitude until somewhere between 10 and 15 diameters aft of the most downstream roughness element. Then, the peak grows weakly in amplitude and stays relatively constant in its location in the boundary layer. Due to the limitations in the measurement region, it is unknown if this streak amplitude would continue growing downstream or if it saturates and then decays.

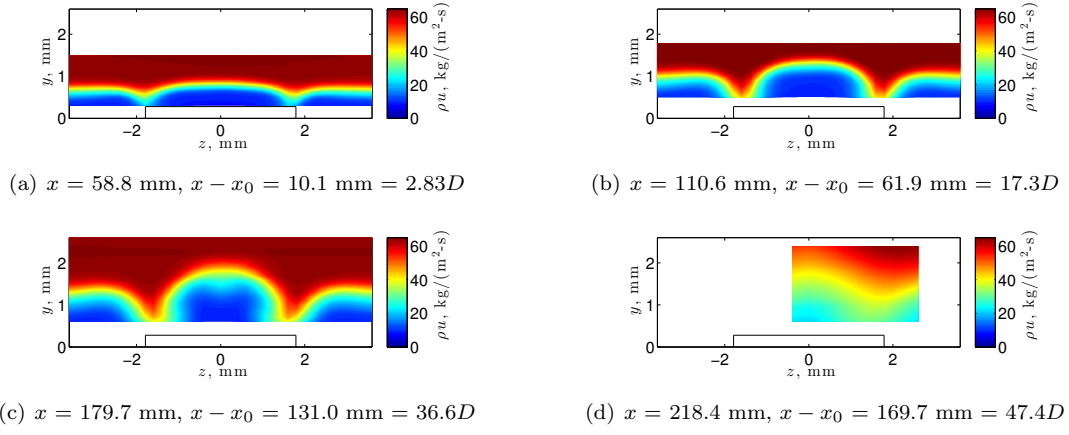


Figure 17. Mean mass flux behind two CREs, spaced $2D$ apart, with the last element centered at $x_0 = 48.7$ mm ($k \approx 280$ μ m).

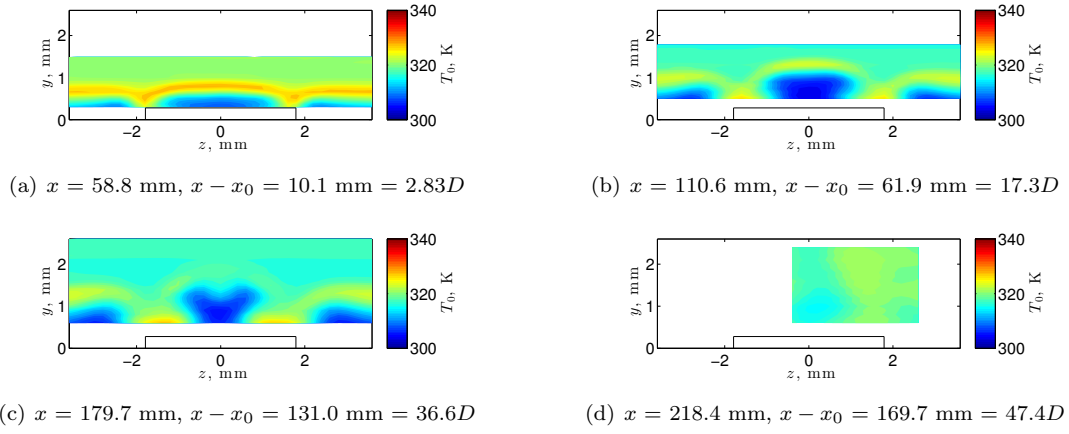


Figure 18. Mean total temperature behind two CREs, spaced $2D$ apart, with the last element centered at $x_0 = 48.7$ mm ($k \approx 280$ μ m).

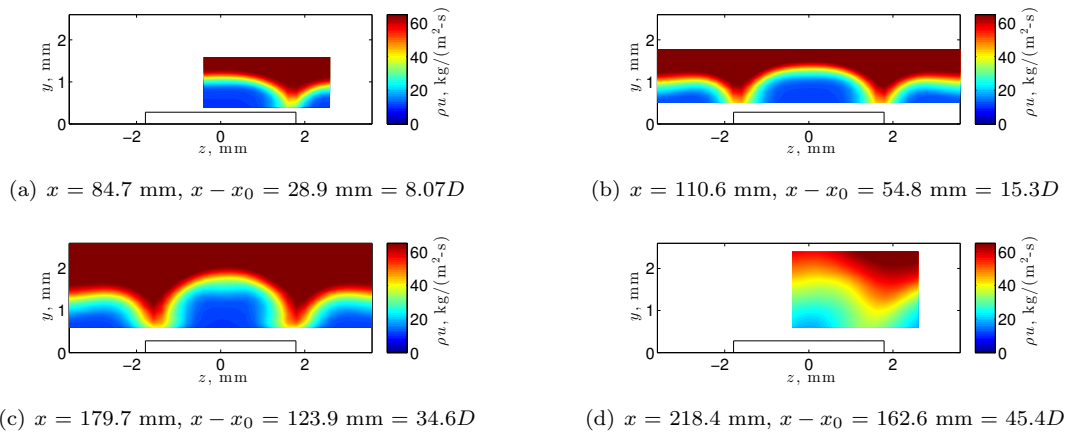


Figure 19. Mean mass flux behind three CREs, spaced $2D$ apart, with the last element centered at $x_0 = 55.8$ mm ($k \approx 280$ μ m).

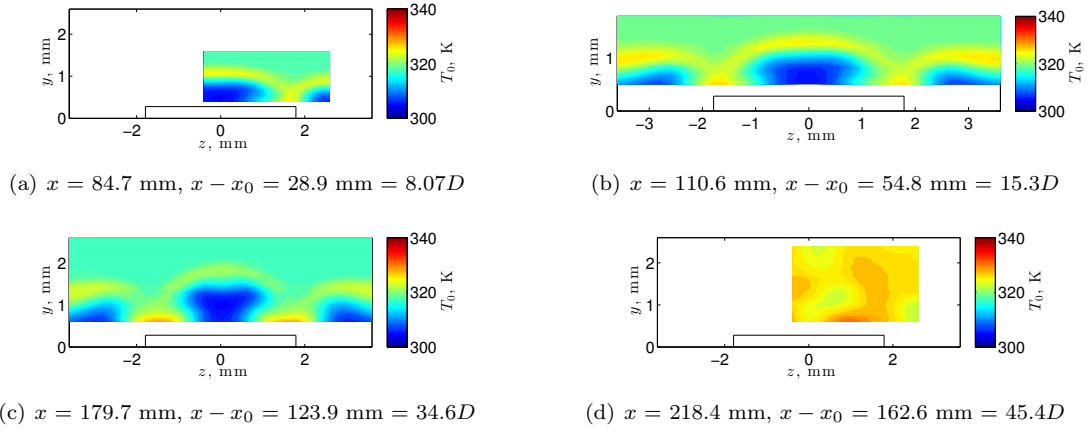


Figure 20. Mean total temperature behind three CREs, spaced $2D$ apart, with the last element centered at $x_0 = 55.8$ mm ($k \approx 280$ μm).

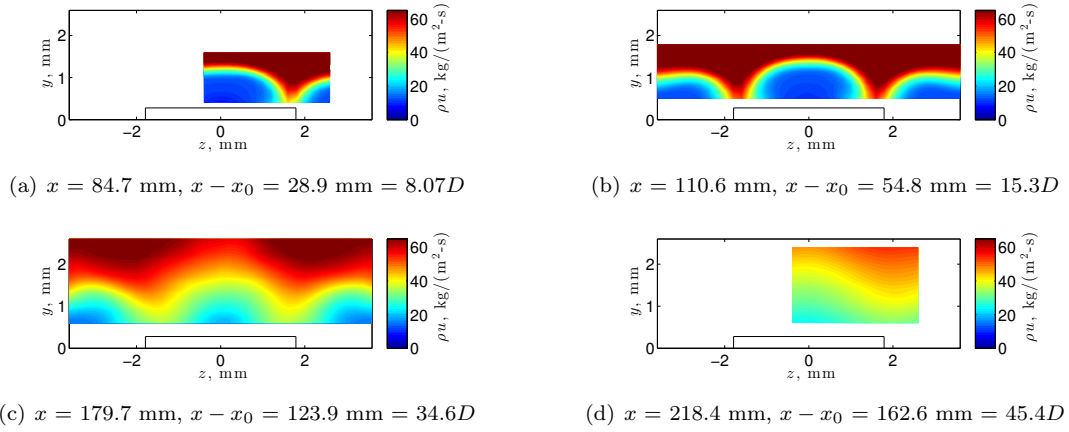


Figure 21. Mean mass flux behind two CREs, spaced $4D$ apart, with the last element centered at $x_0 = 55.8$ mm ($k \approx 280$ μm).

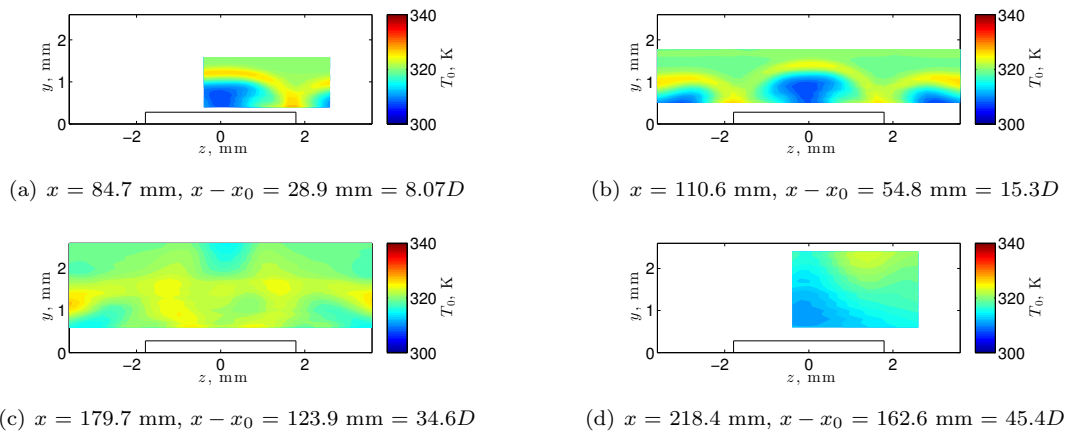


Figure 22. Mean total temperature behind two CREs, spaced $4D$ apart, with the last element centered at $x_0 = 55.8$ mm ($k \approx 280$ μm).

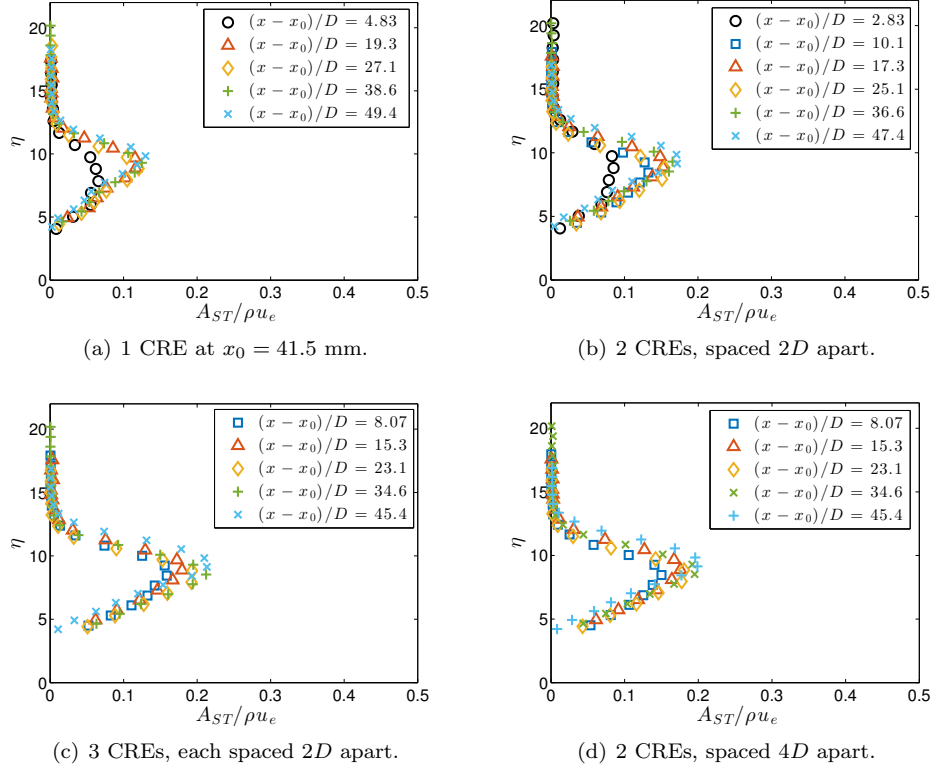
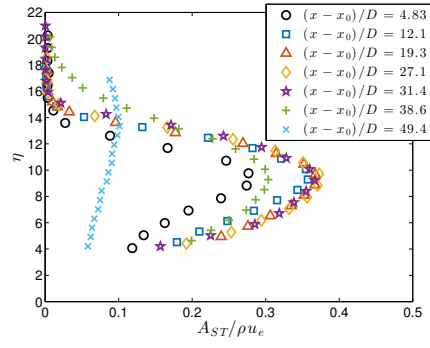


Figure 23. Streak strength profiles for CREs in a streamwise array ($k \approx 140 \mu\text{m}$).

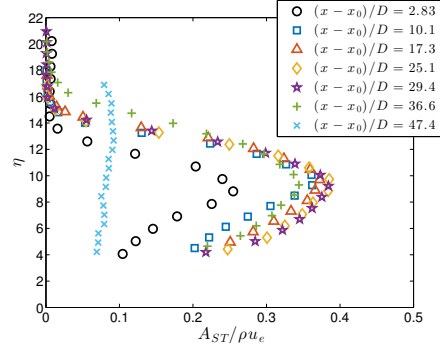
Fig. 24 shows the streak strength profiles behind the arrays of $280\text{-}\mu\text{m}$ -tall CREs. The maximum in streak strength increases as measurements are taken farther downstream of the array of roughness elements. The $280\text{-}\mu\text{m}$ elements have a peak in the streak strength profiles that appears broader than the peak seen in the streak strength profiles taken from behind the $140\text{-}\mu\text{m}$ elements. The streak strength profile then begins to broaden even further at locations farther downstream than 30 diameters. Unlike the streak strength profiles behind the $140\text{-}\mu\text{m}$ elements, the streak strength profiles behind the $280\text{-}\mu\text{m}$ elements flatten out at the farthest downstream measurement stations. These streak strength profiles for the wider spacing of two CREs (Fig. 24(d)) appears to broaden and flatten well before the other configurations of streamwise arrays (Figs. 24(a), 24(b), and 24(c)). This effect indicates that the streak amplitude has decreased, and the relative mean flow distortion is less.

Plots of the streak amplitudes at the different streamwise measurement stations are compared by plotting the maximum streak strength for each location against the distance downstream of the most aft roughness element in the array. The downstream distance is normalized by the number of diameters (D) in the following plots. A comparison of the streak strengths of the different cylindrical roughness configurations in Fig. 25 shows that both the spacing and the heights of the roughness elements determine the strength of the streaks behind the cylindrical roughness array. For a given cylindrical roughness that is $140 \mu\text{m}$ tall, there is weak growth over the streamwise extent of the measurement region (Fig. 25(a)). This indicates that the relative amplitude of the streaks does not change much in the downstream measurement region. The addition of the number of roughness elements in the array appears to create an increase in the amplitude of the streaks. However, a comparison of the array of three circles spaced $2D$ apart and the array of two circles spaced $4D$ apart in Fig. 25(a) shows little change in the streak amplitude. For roughness elements that are approximately $140 \mu\text{m}$ tall, the streak amplitude appears to be affected by the position of the most upstream and most downstream element in the streamwise array rather than the number of elements in the array itself.

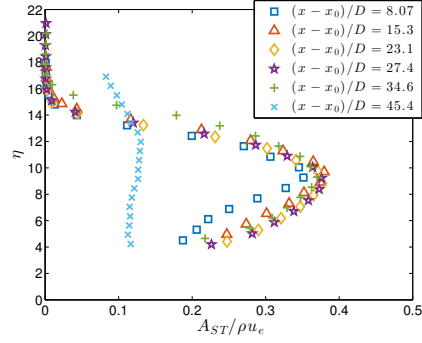
As expected, an increase in the height of the CRE produces an increase in the streak amplitude (Fig. 25(b)). Roughness elements that are $280 \mu\text{m}$ tall produce a streak amplitude that rapidly increases with downstream distance, saturates, and then decays as the wake breaks down. However, when they are spaced $2D$ apart,



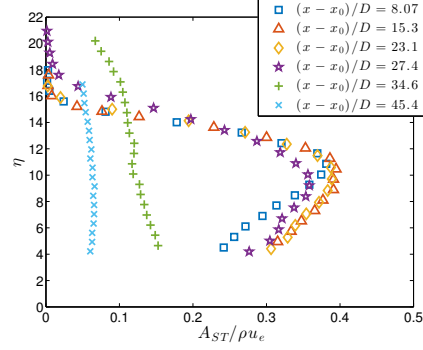
(a) 1 cylindrical roughness at $x_0 = 41.5$ mm.



(b) 2 CREs, spaced $2D$ apart.

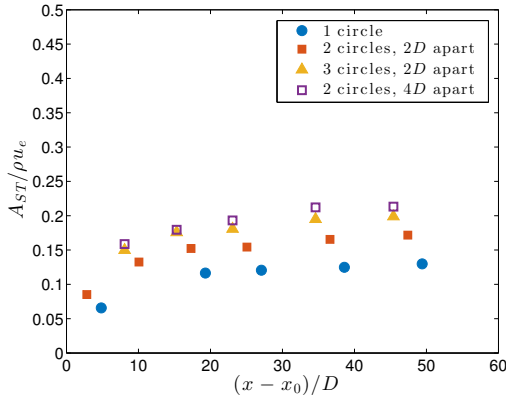


(c) 3 CREs, each spaced $2D$ apart.

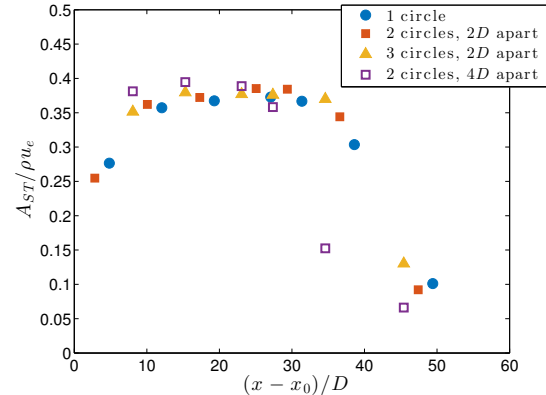


(d) 2 CREs, spaced $4D$ apart.

Figure 24. Streak strength profiles for CREs in a streamwise array ($k \approx 280 \mu\text{m}$).



(a) $k = 140 \mu\text{m}$.



(b) $k = 280 \mu\text{m}$.

Figure 25. Streak amplitudes as a function of downstream measurement location of CREs with different heights and separations.

the number of CREs in a streamwise array does not appear to affect the streak amplitude at the different measurement stations downstream of the last roughness element. The wider spacing of the roughness elements at $4D$ apart appears to decrease the streak strength much faster than a spacing of $2D$ apart. Here, the spacing of the roughness elements appears to have less of an effect on the streak amplitude initially, but produces the rapid decrease in streak strength much sooner when spaced $4D$ apart as opposed to $2D$ apart. This effect is due to the wake breaking down earlier behind the roughness elements with wider spacing, as will be shown in the next section.

C. Contour Plots of RMS Mass-Flux Fluctuations

In the configurations with shorter roughness heights, the locations where the maximum mass flux fluctuation occurred was not easily found in the spectra, but were more obvious in the contour plots of RMS mass-flux fluctuations. These contour plots showed the regions where higher-amplitude instabilities were concentrated more clearly. The mode shapes of the boundary layer instabilities at one of the farthest downstream measurement stations were given by contour plots shown in Fig. 26. Here, the shape of the contours suggest the presence of an odd mode (sinuous) instability.²

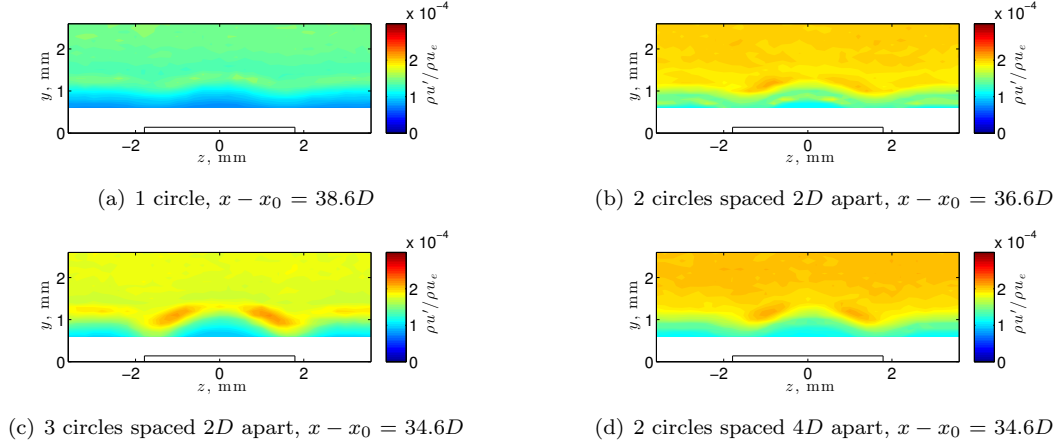


Figure 26. Contour plot of RMS mass-flux fluctuations at $x = 179.7$ mm centered around 45 kHz behind roughness elements ($k = 140$ μm).

These mode shapes are not detectable above the noise floor of the anemometer for the measurement stations farther upstream. The 140- μm roughness height does not appear to generate large instabilities in the usable measurement regions on the flat plate. In fact, the case with a single 140- μm -tall roughness does not show clear signs of the instability mode that is present in the other cases. Even in the case of two 140- μm -tall roughness elements spaced $2D$ apart, it is difficult to distinguish the presence of these modes against the background content.

Measurements of an instability mode behind the 280- μm -tall roughness elements are presented in Figs. 27, 28, 29, and 30. Note that the range on the contour plot had to be adjusted by more than two orders of magnitude for these plots as compared to the contour plots shown in Fig. 26. These contour plots show a symmetric (even) mode that grows and becomes nonlinear at some streamwise station in the measurement region. Full plane measurements were taken at some locations ($x = 110.6$ mm and $x = 179.7$ mm), but once it was established that the flow field was fairly symmetric, half-plane measurements were taken at intermediate locations.

The addition of roughness elements spaced $2D$ downstream appears to have little effect, and even causes the amplitude of the mass-flux fluctuations to decrease at a given x -location. Note that the locations of these planar surveys were held constant relative to the leading edge of the flat plate, so they shift closer to the last roughness element with each addition to the streamwise array. At $x = 179.7$ mm (Figs. 27(e), 28(e), and 29(e)), the shape of the instability mode appears to become distorted. This distortion may be an indication of the instability mode becoming nonlinear at this station, and then breaking down by the last measurement plane at $x = 218.4$ mm (Figs. 27(f), 28(f), and 29(f)).

Contour plots of the RMS mass-flux fluctuations are shown in Fig. 30 for planes at several downstream stations behind two CREs spaced $4D$ apart. These contour plots continue to illustrate an even-mode instability that grows downstream of the last roughness element. By the measurement location in Fig. 30(d), the instabilities start to exhibit some nonlinear attributes, such as a distorted shape compared to the linear eigenmodes. The distorted mode shape at this location appears more upstream than for the roughness arrays that have elements spaced $2D$ apart. The maximum amplitude of this instability occurs on the centerline and is approximately half an order of magnitude larger than the case with three CREs spaced $2D$ apart at the same measurement location ($27.4D$ downstream of the most aft roughness). Near the measurement location in Fig. 30(e), the flow begins to break down. At the measurement location in Fig. 30(f), the flow is fairly turbulent and no clear eigenmodes are visible. This indicates that transition likely occurs sooner for

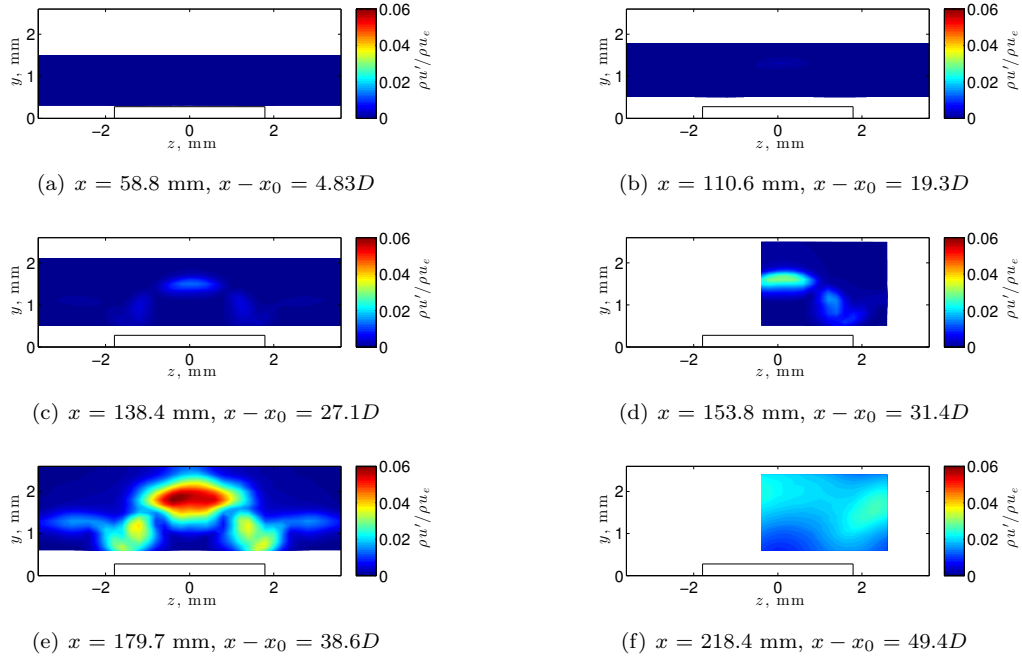


Figure 27. RMS mass-flux fluctuations at the most amplified frequency (80 ± 2.5 kHz) normalized by the edge mass flux behind a single CRE ($k \approx 280$ μm).

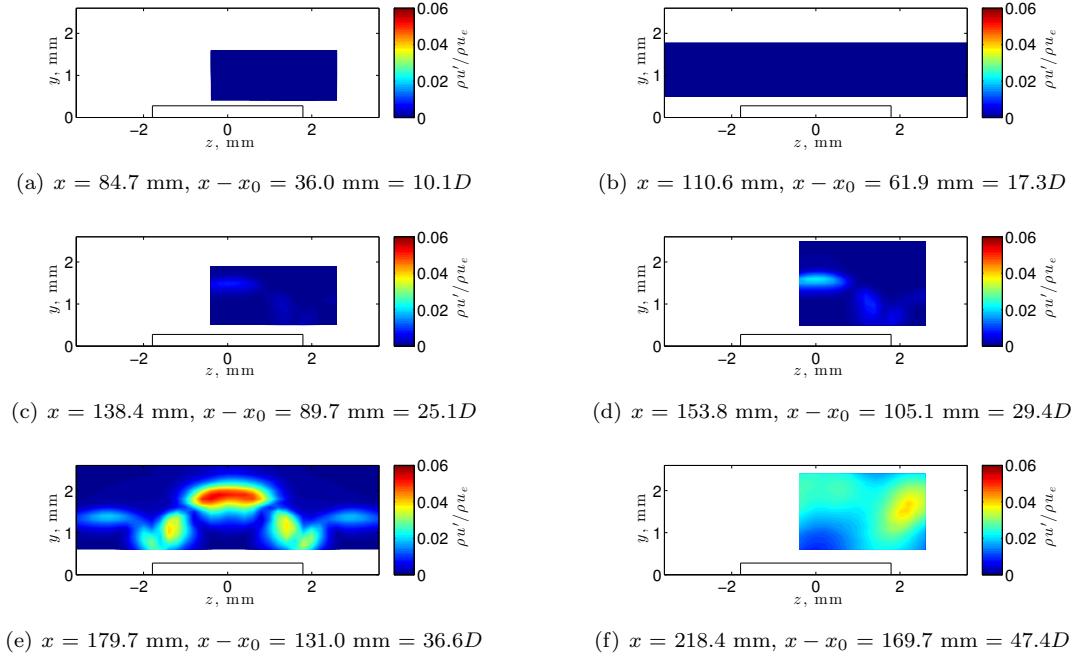


Figure 28. RMS mass-flux fluctuations normalized by the edge mass flux for a 5 kHz band centered at 75 kHz behind two CREs ($k \approx 280$ μm), spaced $2D$ apart.

the array that is arranged $4D$ apart than for the array arranged $2D$ apart.

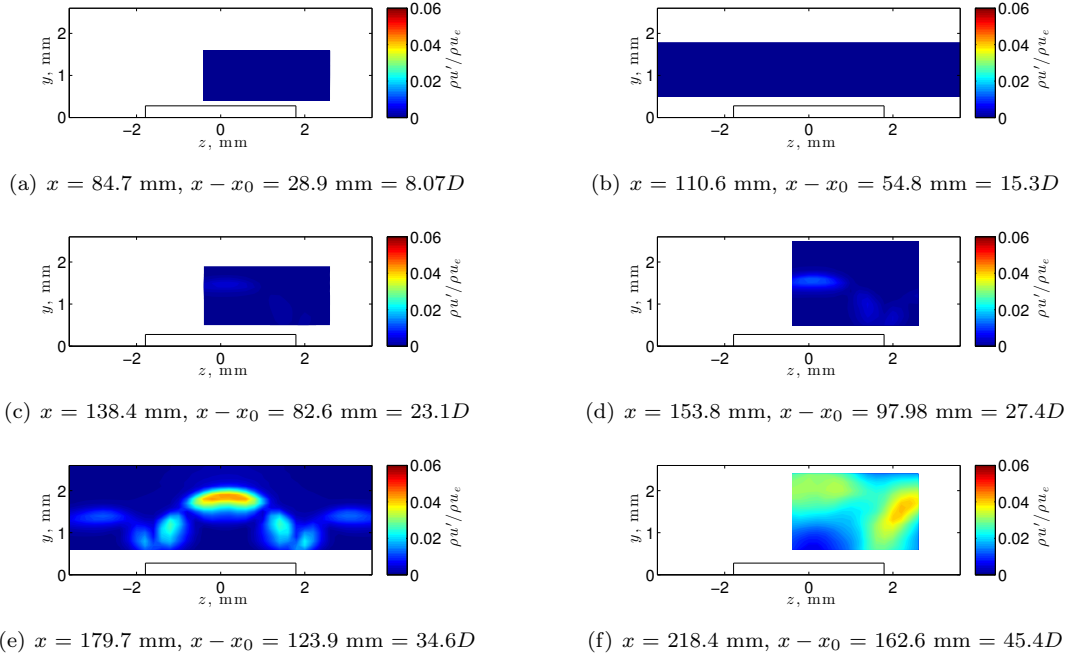


Figure 29. RMS mass-flux fluctuations normalized by the edge mass flux for a 5 kHz band centered at 75 kHz behind three CREs ($k \approx 280$ μm), spaced $2D$ apart.

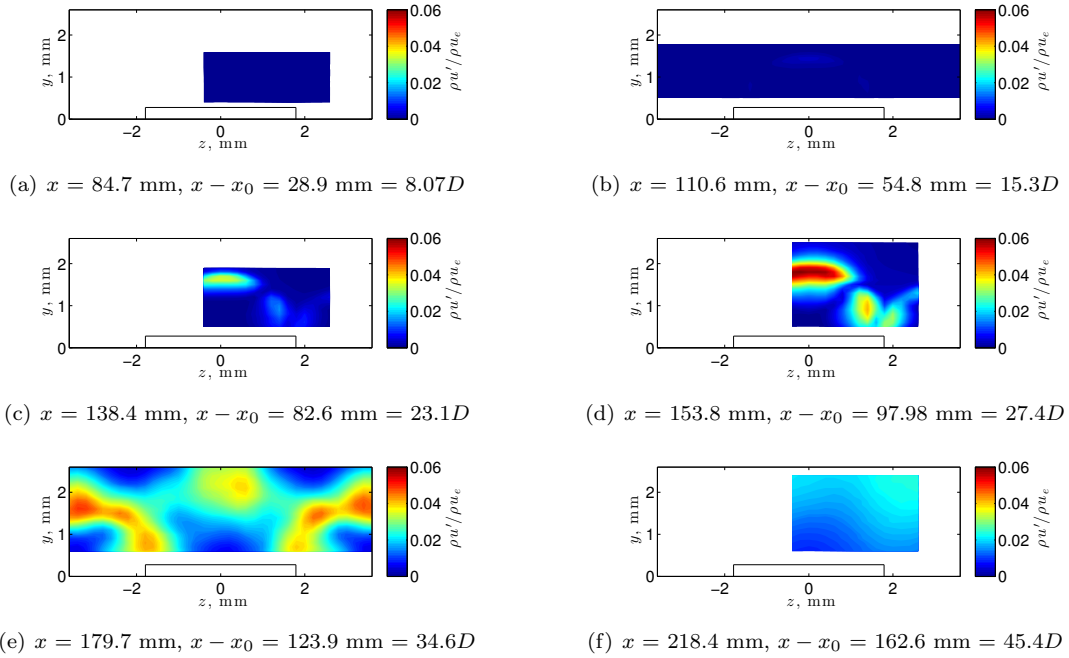


Figure 30. RMS mass-flux fluctuations normalized by the edge mass flux for a 5 kHz band centered at 80 kHz behind two CREs ($k \approx 280$ μm), spaced $4D$ apart.

D. Power Spectra of Mass-Flux Fluctuations at Downstream Locations

The frequency band that appeared to provide the most obvious contours of instability were used to determine where the RMS mass-flux fluctuations reached a maximum, particularly for the shorter of the roughness heights tested. The spectra from these locations were then compared at each streamwise measurement station. The plots in Fig. 31 show the power spectra of the mass flux fluctuation at the location where the greatest RMS mass flux fluctuation was measured. A very small peak above the electronic noise floor is visible at about 45 kHz in some of the spectra, however the spectra do not show clear signs of this being an instability in the flow. The low frequency content (between 1 and 10 kHz) remains fairly low near the roughness element, up to approximately $15D$ or $17D$ downstream. Then the power in this low frequency band rises as the measurement distances increases downstream of the roughness element. This low frequency content is likely a contribution from the freestream, as it is often observed in the empty tunnel. There is also a peak at approximately 18 kHz, but this peak appears in the spectra for other flow conditions and roughness configurations, so it is not clear that this is related to the cylindrical roughness arrays. Fig. 31(c) shows a slightly different noise floor at $(x - x_0)/D = 15.3$, which was due to an unintentional change in the anemometer bridge tuning for that particular run.

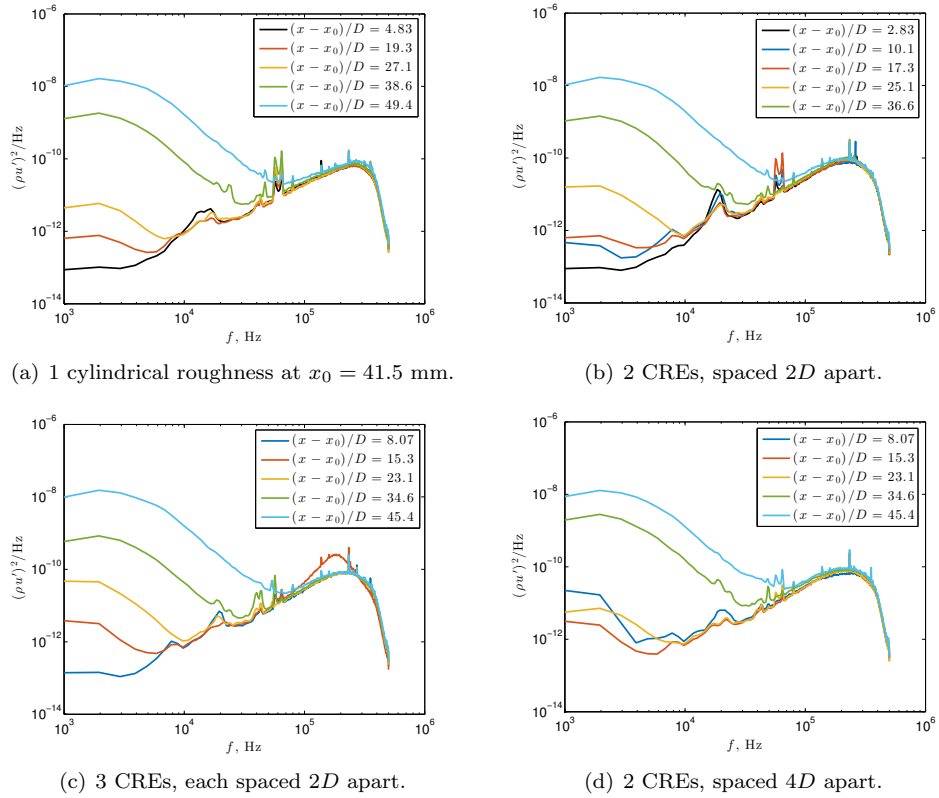


Figure 31. Power spectra of the mass-flux fluctuations behind streamwise arrays of CREs ($k \approx 140 \mu\text{m}$).

A comparison of the RMS amplitudes of the mass-flux fluctuations at the different streamwise stations for the different roughness configurations are given in Fig. 32. These RMS amplitudes are all roughly the same magnitude for each configuration. As a result, there is not a clear difference in the effect of these configurations on the instabilities or transition downstream of the roughness. These RMS amplitudes also do not appear to grow within the length of the measurement region.

Although it was not necessary to use the contour plots to determine the dominant frequency of the instability behind the $280\text{-}\mu\text{m}$ -tall roughness elements, the RMS contours were still used to find the peak RMS at each measurement station and the corresponding spectra are plotted in Fig. 33. An instability peak, centered around 75 or 80 kHz, is clearly visible in the spectra for the taller of the roughness elements tested. This peak grows with the measurement distance from the last roughness element until the spectra broaden. As the frequency content across the full bandwidth starts to fill in, the peak in the spectra begins

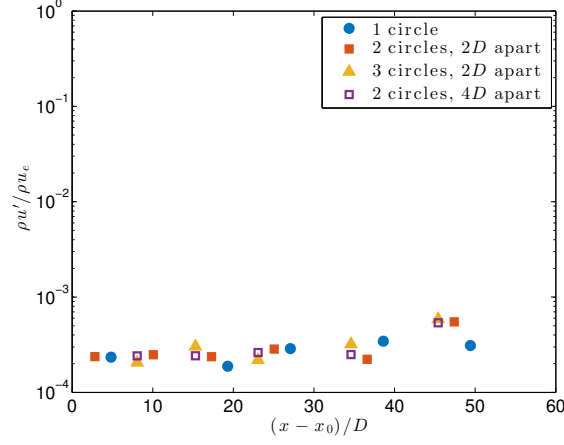


Figure 32. Maximum RMS mass-flux fluctuations centered around 45 kHz behind different roughness configurations: $k \approx 140 \mu\text{m}$, $p_0 = 207.0 \text{ kPa}$, $T_0 = 319.3 \text{ K}$.

to diminish. For the case with two CREs spaced $4D$ apart (Fig. 33(d)), the peak disappears completely at the most downstream station and the spectra are indicative of a broadband, turbulent signal.

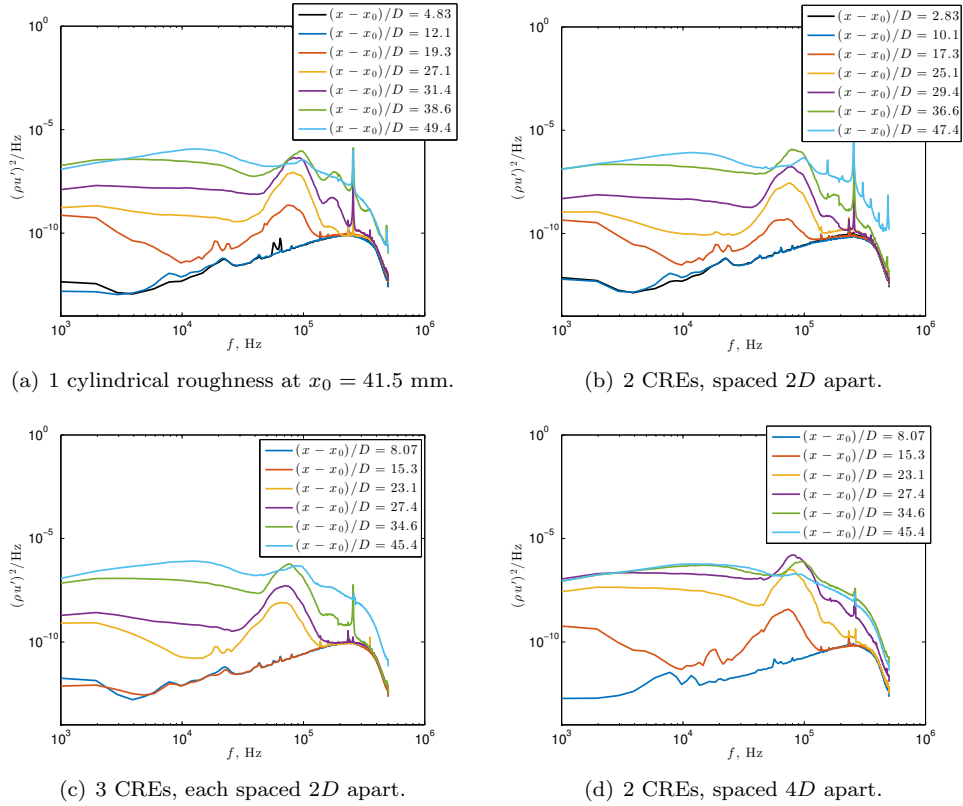


Figure 33. Power spectra of the mass-flux fluctuations behind streamwise arrays of CREs ($k \approx 280 \mu\text{m}$).

The RMS mass-flux fluctuations centered around the peak instability are given by Fig. 34. The mass-flux fluctuations reach a peak somewhere along the centerline of the flat plate behind the roughness element. When the locations of the RMS amplitudes of the mass-flux fluctuations are normalized by the number of diameters from the most downstream roughness element, the data appear to collapse onto one curve for roughness elements spaced $2D$ apart. The data for the roughness elements that were spaced $4D$ apart do

not follow the same curve. In fact, the data indicate that the roughness elements that are spaced $4D$ apart cause transition onset to occur approximately $10D$ farther upstream.

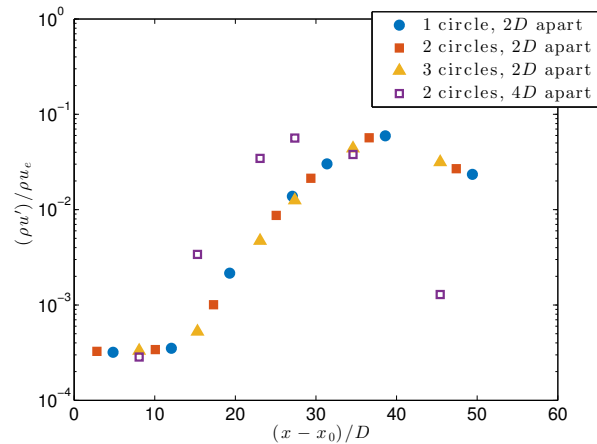


Figure 34. Maximum RMS mass-flux fluctuations centered around the most amplified frequency behind different roughness configurations: $k = 280 \mu\text{m}$, $p_0 = 206.8 \text{ kPa}$, $T_0 = 319.3 \text{ K}$.

V. Summary

Cylindrical roughness elements were placed on the surface of a flat plate and arranged in a streamwise array. The cylindrical roughness elements were approximately $140 \mu\text{m}$ and $280 \mu\text{m}$ tall and arranged in configurations with up to three roughness elements spaced $2D$ and $4D$ apart. As additional roughness elements spaced $2D$ were added downstream of the $280 \mu\text{m}$ cylindrical roughness, the onset of transition did not move relative to the location of the most downstream roughness element. The two roughness elements spaced $4D$ apart showed a forward shift in transition location by approximately $10D$ relative to the most downstream roughness in the streamwise array.

The heights and spacing of roughness elements on the surface of a flat plate determine the effectiveness of their ability to trip the flow. This information is similar to that seen by Choudhari et al.,²² whose computations show that the heights of tandem roughness elements affects the streak amplitude. Choudhari et al. found that the shorter roughness elements in their computations had an effect on the streak amplitude because the flow was able to recover after the first roughness and perturbed the incoming flow to the second downstream roughness in order to create larger streak amplitudes. The taller roughness elements in Choudhari et al.'s computations did not have as much of an effect on the streak amplitudes because the wake behind the first roughness element had not recovered by the time the flow reached the second roughness element. A similar effect may be occurring here, where the $2D$ spacing does not allow the wake to recover behind upstream roughness elements, so the streamwise array of elements has the same effect as a single roughness. The $4D$ spacing may allow for the wake to recover after the most upstream roughness so that both roughness elements have an effect.

VI. Acknowledgments

This work was made performed under the Revolutionary Computational Aerosciences discipline under the Transformational Tools and Technologies Project of the NASA Fundamental Aeronautics Program. The authors would also like to thank Rhonda Mills and Ricky Clark for their support of the wind tunnel testing.

References

- ¹Casper, K. M., Wheaton, B. M., Johnson, H. B., and Schneider, S. P., "Effect of Freestream Noise on Roughness-Induced Transition for a Slender Cone," *Journal of Spacecraft and Rockets*, Vol. 48, No. 3, May–Jun 2011, pp. 406–413.
- ²Choudhari, M., Li, F., Chang, C.-L., Norris, A., and Edwards, J., "Wake Instabilities behind Discrete Roughness Elements

in High Speed Boundary Layers,” AIAA Paper 2013–0081, January 2013.

³Wheaton, B. M. and Schneider, S. P., “Roughness-Induced Instability in a Hypersonic Laminar Boundary Layer,” *AIAA Journal*, Vol. 50, No. 6, Jun 2012, pp. 1245–1256.

⁴Wheaton, B. M. and Schneider, S. P., “Hypersonic Boundary-Layer Instabilities due to Near-Critical Roughness,” *Journal of Spacecraft and Rockets*, Vol. 51, No. 1, Jan–Feb 2014, pp. 327–342.

⁵Kegerise, M. A., King, R. A., Owens, L. R., Choudhari, M. M., Norris, A. T., Li, F., and Chang, C.-L., “An Experimental and Numerical Study of Roughness-Induced Instabilities in a Mach 3.5 Boundary Layer,” Tech. rep., NATO RTO AVT-200 RSM-030 Specialists’ Meeting on Hypersonic Laminar-Turbulent Transition, April 2012.

⁶Kegerise, M. A., King, R. A., Choudhari, M., Li, F., and Norris, A., “An Experimental Study of Roughness-Induced Instabilities in a Supersonic Boundary Layer,” AIAA Paper 2014–2501, June 2014.

⁷Reibert, M. S., Saric, W. S., Jr., R. B. C., and Chapman, K. L., “Experiments in nonlinear saturation of stationary crossflow vortices in a swept-wing boundary layer,” AIAA Paper 1996–0184, January 1996.

⁸Saric, W. S., Jr., R. B. C., and Reibert, M. S., “Leading-edge roughness as a transition control mechanism,” AIAA Paper 1998–0781, January 1998.

⁹Saric, W. S., West, D. E., Tufts, M. W., and Reed, H. L., “Flight Test Experiments on Discrete Roughness Element Technology for Laminar Flow Control,” AIAA Paper 2015–0539, January 2015.

¹⁰Owens, L. R., Beeler, G. B., Balakumar, P., and McGuire, P. J., “Flow Disturbance and Surface Roughness Effects on Cross-Flow Boundary-Layer Transition in Supersonic Flows,” AIAA Paper 2014–2638, June 2014.

¹¹Schuele, C. Y., Corke, T. C., and Matlis, E. H., “Control of Stationary Cross-Flow Modes in a Mach 3.5 Boundary Layer Using Patterned Passive and Active Roughness,” *Journal of Fluid Mechanics*, Vol. 718, February 2013, pp. 5–38.

¹²Ward, C. A., Henderson, R. O., and Schneider, S. P., “Possible Secondary Instability of Stationary Crossflow Vortices on an Inclined Cone at Mach 6,” June 2015.

¹³Chou, A., Ward, C. A., Letterman, L. E., Luersen, R. P., Borg, M. P., and Schneider, S. P., “Transition Research with Temperature-Sensitive Paints in the Boeing/AFOSR Mach-6 Quiet Tunnel,” AIAA Paper 2011–3872, June 2011.

¹⁴Chynoweth, B. C., Ward, C. A., Greenwood, R. T., McKiernan, G. R., Fisher, R. A., and Schneider, S. P., “Measuring Transition and Instabilities in a Mach 6 Hypersonic Quiet Wind Tunnel,” AIAA Paper 2014–2643, June 2014.

¹⁵Downs, R. S., White, E. B., and Denissen, N. A., “Transient Growth and Transition Induced by Random Distributed Roughness,” *AIAA Journal*, Vol. 46, No. 2, February 2008, pp. 451–462.

¹⁶Kuester, M. S. and White, E. B., “Distributed-Roughness-Induced Transient Growth in a Flat Plate Boundary Layer,” AIAA Paper 2013–3107, June 2013.

¹⁷Kuester, M. S., White, E. B., Sharma, A., Goldstein, D. B., and Brown, G., “Distributed Roughness Shielding in a Blasius Boundary Layer,” AIAA Paper 2014–2888, June 2014.

¹⁸Drews, S. D., Downs, III, R. S., Doolittle, C. J., Goldstein, D. B., and White, E. B., “Direct Numerical Simulations of Flow Past Random Distributed Roughness,” AIAA Paper–564, January 2011.

¹⁹Sharma, A., Drews, S. D., Kuester, M., Goldstein, D. B., and White, E. B., “Evolution of disturbances due to discrete and distributed surface roughness in initially laminar boundary layers,” AIAA Paper 2014–0235, January 2014.

²⁰Suryanarayanan, S., Goldstein, D. B., Brown, G. L., Berger, A. R., and White, E. B., “On the Mechanics and Control of Boundary Layer Transition Induced by Discrete Roughness Elements,” AIAA Paper 2017–0307, January 2017.

²¹Carmichael, B. H., “Critical Reynolds Numbers for Multiple Three Dimensional Roughness Elements,” Report number NAI-58-589 (BLC-112), Northrop Aircraft, Inc., Hawthorne, CA, Jul 1958.

²²Choudhari, M., Li, F., Wu, M., Chang, C.-L., Edwards, J., Kegerise, M., and King, R., “Laminar-Turbulent Transition behind Discrete Roughness Elements in a High-Speed Boundary Layer,” AIAA Paper 2010–1575, January 2010.

²³Kegerise, M. A., Owens, L. R., and King, R. A., “High-Speed Boundary-Layer Transition Induced by an Isolated Roughness Element,” AIAA Paper 2010–4999, June 2010.

²⁴Fransson, J. H., Brandt, L., Talamelli, A., and Cossu, C., “Experimental and Theoretical Investigation of the Nonmodal Growth of Steady Streaks in a Flat Plate Boundary Layer,” *Physics of Fluids*, Vol. 16, No. 10, Oct 2004, pp. 3627–3638.